INSTITUTE OF PHYSICS PUBLISHING JOURNAL OF MICROMECHANICS AND MICROENGINEERING
J. Micromech. Microeng. **12** (2002) 898–904 PII: S0960-1317(02)36231-4

Photo-injection based sample design and electroosmotic transport in microchannels

David Sinton, David Erickson and Dongqing Li

Department of Mechanical and Industrial Engineering, University of Toronto, 5 King's College Road, Toronto, ON, Canada M5S 3G8

E-mail: dli@mie.utoronto.ca

Received 25 April 2002, in final form 2 September 2002
Published 7 October 2002
Online at stacks.iop.org/JMM/12/898

Abstract
Techniques for facilitating chemical reactions and transporting reactants in microfluidic applications are becoming increasingly important. Combined experimental and numerical studies of a photochemical injection process and the subsequent electroosmotic transport of products are presented here. In the experiments, intense focusing of ultraviolet light performs local photolysis of a caged fluorescent dye in a 25 μm i.d. capillary. The advection and diffusion of this sample in electroosmotic flow are imaged using a micro-flow visualization system. Independent numerical simulations of the sample transport are conducted with a custom-designed code. Strong agreement between the numerical predictions and the experimental results is established. Further comparisons demonstrate that near-ideal, diffusion-limited sample transport has been achieved. Focusing on diffusion, numerical simulations show that alternative sample concentration profiles may be obtained through the diffusive interactions of multiple, photo-injected Gaussian sample concentration profiles. In particular, a compact, flat-topped sample profile, exhibiting a constant concentration plateau is predicted. The ability to produce this sample profile using multiple photo injections was demonstrated experimentally in agreement with numerical simulation results.

1. Introduction

The proliferation of manufacturing techniques for building microfluidic components has led to a virtual explosion in the development of microscale chemical and biological analysis systems, which collectively fall under the lab-on-chip concept. Electroosmotic flow, where an applied electric potential difference induces fluid motion, is becoming more and more common as a method of fluid transport in such devices. However, as these microfluidic technologies mature from simple geometries into extensive microfluidic networks, exact control over chemical reactions and species transport becomes critical. In the laboratory, a wide range of chemical reactions, both chain and non-chain, can be accomplished using light as a reagent including oxidation/reduction; photolysis; photohydrolysis; photoionization; molecular rearrangements; addition and elimination, dimerization and polymerization [1, 2].

Photochemical reactions have proved useful in high-performance liquid chromatography (HPLC) [1, 3]. In HPLC, compounds are separated in a packed column due to differential sorptive properties. Accurate detection of analytes as they exit the column sometimes requires derivatization. This traditionally involves addition of one or more chemical reagents to transform the separated analyte into a more detectable one. Although results vary between analytes, several studies report significant increase in signal-to-noise ratio using photochemical derivatization techniques [2–5]. Microscale liquid chromatography (micro-LC) has recently received much interest due to advantages common to miniaturization: higher speed, lower volume requirements and higher resolution. Lores *et al* [2] designed a post-column

micro-LC photo-reactor that provided signal-to-noise increases of up to 20 fold.

Using light as a reagent can offer many advantages over chemical reagents, namely, it is inexpensive; it acts quickly (as mixing is not required); photons do not introduce decomposition products or residues; the analyte is not diluted (as light is introduced without a solvent) and the intensity of light is easily controlled, independent of the flow properties [1, 2]. Perhaps the most important advantages, with respect to microfluidic applications, stem from the user-interface characteristics. Simply focusing light through a microchannel can invoke a photochemical reaction. Although this typically requires specialized optics and light-transmitting channels, injection of a chemical reagent requires a complete and separate fluid circuit [6, 7]. Although in principle many sample shapes of profiles may be obtained, control is made awkward by the coupling of reservoir potentials through the electric field. Crabtree *et al* [7] discussed many of the challenges encountered using this injection technique.

The advent of photo-liable caged compounds has created the possibility of selectively introducing a specific species by exposing a solution to a specific wavelength of light. The so-called photo-injection techniques serve to extend the applicability of photochemical techniques in microfluidics and mitigate the difficulties associated with mechanical injection. Exposure to a specific wavelength of light breaks the caging groups releasing the desired species. For the purposes of this study, a caged fluorophore was a convenient choice, allowing visualization of the chemical production process and subsequent transport. Similar photo-liable caged fluorescent probes have been previously applied to flow visualization [8–11]. However, molecular probes offer a wide range of caged, biologically-active molecules, including caged nucleotides, chelators, second messengers and neurotransmitters. In conjunction with an appropriate light source, these products can produce concentrated, pico-litre sized injections with minimal infrastructure. The concentration and sample shape are adjustable through altering the beam intensity and geometry. This sample design flexibility afforded by photo-injection techniques can be applied to the generation of alternative sample shapes or specific sample gradients for a variety of applications. A microfluidic network for generation of cross-stream gradients was presented by Dertinger *et al* [12]. They note that gradients of diffusible substances having chemoattractant or chemorepellent properties play a key role in many biological processes, and conventional mechanical injection techniques lack the appropriate accuracy and stability required.

There are two common modes of transporting bulk fluids through microchannels: pressure-driven flow and electroosmotic flow. In channels of circular cross-section, a balance of shear and pressure forces results in the parabolic Poiseuille velocity profile. With respect to discrete sample transport, this flow causes significant sample dispersion due to the radial gradients of advective flux. This leads to high radial concentration gradients and high rates of ordinary diffusion in the radial direction [13]. Sample dispersion, caused by this combination of advection and diffusion (termed Taylor dispersion), makes pressure-driven flow undesirable in most sample transport applications. Electroosmotic flow results in a flat, plug-like velocity profile, that is typically more amicable to sample transport than that of pressure-driven flow [14]. However, an undesirable pressure-driven component may be induced by a number of factors including non-uniformity of surface charge (ζ potential) either in cross-section or axially; a narrowing or partial blockage anywhere in the channel; the presence of charged particles in the fluid; capillary forces resulting from different curvatures of the free surfaces in the reservoirs; contact angle hysteresis of a bubble entrapped in the channel; a non-uniform wall surface charge distribution and slight height differences between the free surfaces in the reservoirs. Sensitivity to these factors is highly correlated with the capillary radius.

The experimental results here show effective diffusion-limited dispersion behavior. This was achieved through careful balancing of reservoirs, removal of bubbles, use of small i.d. capillaries, extensive filtering and application of moderate electrical fields. In this paper, firstly, we demonstrate sample transport with dispersion limited to axial diffusion (in the absence of cross-stream velocity gradients) and establish strong agreement between experiment and numerical analysis. Secondly, we demonstrate how sample shape design (afforded by photochemical processes) can produce non-Gaussian sample profiles with a plateau region of constant concentration. This was achieved experimentally by using multiple photo injections and the results are in agreement with numerical predictions.

2. Experiment

In our experiment, ultraviolet laser light is focused into a sheet crossing the capillary (perpendicular to the flow direction). The resulting uncaged fluorescent dye is continuously excited and the emission is transmitted through a laser-powered epi-illumination microscope. Full frame images of the transport are recorded by a progressive scan CCD camera and stored in a computer.

2.1. Imaging apparatus

A schematic diagram showing flow module and the three light interactions (the ultraviolet uncaging light pulse, the continuous blue excitation light and the resulting green fluorescent emission) is given in figure 1. The ultraviolet light was provided by a 300 μJ, 337 nm, pulsed nitrogen laser. This beam was reflected upwards through a vertical optical rail assembly containing two, counter-oriented cylindrical optics. By manipulating these optics, the geometry of the photo-injected sample could be customized. The continuous flood of excitation light was provided by a single-line, 200 mW, 488 nm argon laser, through the 25×, NA = 0.75, oil immersion microscope objective.

2.2. Image acquisition

A four-channel delay generator controlled the firing of the nitrogen laser and run frequency. The camera was run in video mode and the delay generator fired the laser at convenient intervals. To increase the amount of uncaged dye, the nitrogen laser was pulsed multiple times (at 30 Hz) at each uncaging event. The excitation laser ran unshuttered,

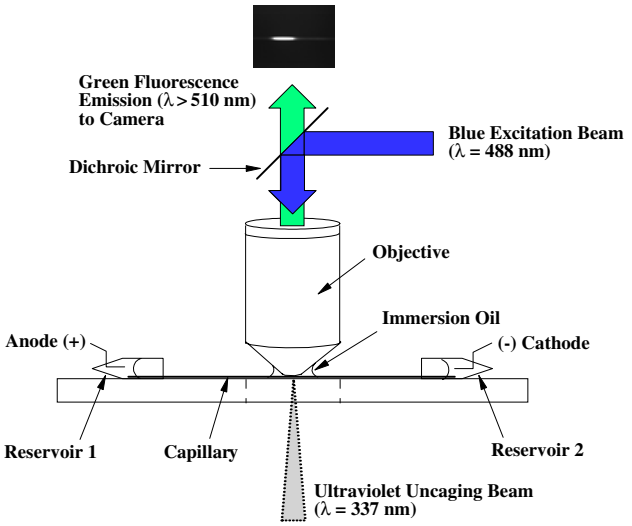

Figure 1. Schematic diagram of the flow module and the three light interactions.

continuously flood-illuminating the capillary. The camera was run at 15 Hz with individual exposure times of 1/125 s. The acquired images had a resolution of 640 × 484 pixels. This corresponded to a 543 μm visible length of capillary, with each pixel representing a 0.85 μm square in the object plane. The camera orientation was carefully adjusted such that the pixel grid was aligned with the radial and axial directions.

2.3. Image processing

To remove any non-uniformities present in the imaging system, dark field image subtraction and bright field image normalization were performed with each image [15]. These images were then smoothed using a distance-based 7 × 7 pixel kernel. Finally, the resulting image series was linearly scaled by a single factor to fill the grayscale range. Axial concentration profiles along the centerline are generated directly from pixel intensity values of the processed images based on a previously determined camera response characteristic.

2.4. Flow systems

To facilitate electroosmotic flow, a 14 cm length of capillary joined two small reservoirs with embedded platinum electrodes. The capillary and the upstream reservoir were filled with the caged dye solution, and the downstream reservoir was filled with buffer. All capillaries were fused silica. The nominal inner diameter of the capillaries was 20 μm; however, the actual inner diameters were estimated at 25 μm. New capillaries (as supplied by Polymicro Tech) were prepared by flushing with pure water followed by flushing with buffer. At the capillary midpoint, the exterior polyimide coating was oxidized and removed to create a viewing window.

2.5. Chemicals

The caged fluorescent dye employed here was 5-carboxymethoxy-2-nitrobenzyl (CMNB)-caged fluorescein (826.81 MW). The dye was dissolved to a concentration of 1.0 mM, in sodium carbonate buffer of ionic strength, $I = 0.05$ and pH = 9.0. Immediately before use, all solutions were filtered using 0.2 μm pore size syringe filters.

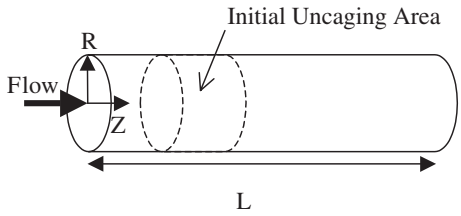

Figure 2. Computational domain for numerical modeling.

3. Computational modeling

In this study we wish to examine the diffusive evolution of a series of sample distributions that are not well represented by analytical functions, particularly in the case of multiple sample interaction as will be discussed later. As a result we have chosen to use a numerical approach to model this behavior. In a number of recent studies, computational fluid dynamics modeling has proven to be an excellent tool for analyzing electrokinetic flow in microfluidic systems and devices. In their work, Ermakov *et al* [6] used a 2D code to model electrokinetic focusing in a microchannel and species mixing at a t-shaped intersection. The results of their computations were shown to be in excellent agreement with experimental results. Bianchi *et al* [16] presented finite element based simulations of combined electroosmotic and pressure-driven flow at a t-intersection. 3D flow simulations were presented by Patankar and Hu [17] who examined the flow behavior at a cross intersection. In another recent study Erickson and Li [18] used 3D thermal simulations to develop an optimized microfluidic device for PCR based DNA amplification as well as 3D flow simulations to model the mixing behavior in a t-shaped channel with heterogeneous surfaces [19]. The theoretical considerations pertaining to the modeling of electroosmotic flow in microchannels have been covered in detail by both Ermakov *et al* [6] and Patankar and Hu [17] and thus here we concentrate primarily on presenting the relevant equations, primary assumptions, simulation conditions and numerical method.

3.1. Basic equations and modeling assumptions

In this section a brief overview of the pertinent modeling equations is presented. For further details on the numerical method, the reader is referred to [19]. In this study we consider microfluidic transport in the axis-symmetric geometry shown in figure 2. Electroosmotic flow results from the interaction of an applied electric field with the non-uniform ion concentrations in the electrical double layer (EDL), and is described by the Navier–Stokes equations subject to an electroosmotic body force and the continuity equation (given below in a non-dimensional form),

$$Re\left[\frac{\partial V}{\partial \tau} + (V \cdot \tilde{\nabla})V\right] = -\tilde{\nabla}P + \tilde{\nabla}^2 V + F_e \qquad (1a)$$

$$\tilde{\nabla} \cdot V = 0 \qquad (1b)$$

where V is the non-dimensional velocity ($V = v/v_0$, where v_0 is a reference velocity), P is the non-dimensional pressure, τ is the non-dimensional time and Re is the Reynolds number given by $Re = \rho v_{eo} L/\eta$ where L is a length scale taken as the channel radius, r_0, in this case. In general, the high voltage requirements limit most practical electroosmotic flows in microchannels to small Reynolds numbers, and therefore to simplify equation (1a), we ignore transient and convective terms and limit ourselves to low Reynolds number cases. F_e represents the non-dimensional electroosmotic body force given by

$$F_e = \left(\frac{\varepsilon_w \phi_{max} k_b T}{z e r_0 \eta v_{eo}}\right)[\tilde{\nabla}^2 \Psi \cdot \tilde{\nabla}\Phi] \qquad (1c)$$

where Ψ represents the non-dimensional EDL field strength ($\Psi = z\psi e/k_b T$, where k_b is the Boltzmann constant, T is the absolute temperature, e is the charge of an electron and z is the ionic valence), Φ is the non-dimensional applied electric field strength ($\Phi = \phi/\phi_{max}$, where ϕ_{max} is the maximum applied voltage), η is the viscosity, ϵ_w is the electrical permittivity of the solution and the $\sim$ symbol over the ∇ operator indicates the gradient with respect to the non-dimensional coordinates ($R = r/r_0$ and $Z = z/r_0$).

As is apparent from equation (1c), full evaluation of the electroosmotic body force requires a description of both Ψ and Φ. Numerical modeling of electrokinetic flow and species transport in microstructures, however, is complicated by the simultaneous presence of three separate length scales; the channel length (mm), the channel radius (μm) and the double layer thickness, $1/\kappa$ (nm). In general, the amount of computational time and memory required to fully capture the complete solution on all three length scales would make such a problem nearly intractable. As is discussed in detail by Erickson and Li [19] the easiest way to alleviate this problem is to set $F_e = 0$ in equation (1a) and apply a slip boundary condition at the channel wall, V_{eo}, given by

$$V_{eo} = \left(\frac{\mu_{eo}\phi_{max} r_0}{v_0}\right)\tilde{\nabla}\Phi = \left(\frac{\varepsilon_w \zeta \phi_{max} r_0}{\eta v_0}\right)\tilde{\nabla}\Phi \qquad (2)$$

where μ_{eo} is the electroosmotic mobility of the surface and ζ is the zeta-potential. By this method the double layer length scale is completely eliminated from the solution domain, and a description of the double layer region is no longer required. A similar slip condition approach was used by Stroock *et al* [20] in their simulations of electrokinetically induced circulating flows and found to be in excellent agreement with experimental results.

As is shown in figure 2, we consider the transport of an initial sample from where it is first released in the 'initial uncaging area' and then transported downstream. Species transport by electrokinetic means is accomplished by three mechanisms, convection, diffusion and electrophoresis, and can be described by equation (3) [9],

$$Pe\left[\frac{\partial C}{\partial \tau} + \tilde{\nabla} \cdot (C(V + V_{ep}))\right] = \tilde{\nabla}^2 C \qquad (3)$$

where C is the non-dimensional species concentration ($C = c/c_0$, where c_0 is a reference concentration species of interest in the buffer solution.), Pe is the Péclet number ($Pe = v_{eo} r_0/D$, where D is the diffusion coefficient) and V_{ep} is the non-dimensional electrophoretic velocity given by

$$V_{ep} = \left(\frac{\mu_{ep}\phi_{max} r_0}{v_0}\right)\tilde{\nabla}\Phi \qquad (4)$$

and μ_{ep} is the electrophoretic mobility. The diffusion coefficient of $D = 4.37 \times 10^{-6}$ cm^2 s^{-1}, as previously suggested for the uncaged fluorescein [9], was found to agree with our measured values and employed here. Calculating the electrophoretic mobility of the dye from the Nernst–Einstein relation gives $\mu_{ep} = -3.3 \times 10^{-4}$ cm^2 V^{-1} s^{-1}. In solving equation (3) a homogeneous fixed boundary condition was used at the inlet and a zero gradient was applied at the outlet.

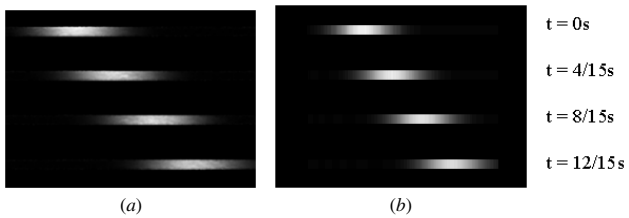

Figure 3. Transport of uncaged fluorescein sample in 25 μm diameter capillary (sequence of images shown at 4/15 s intervals): (*a*) experimental results and (*b*) numerical predictions.

4. Results and discussion

To inject a single sample, the ultraviolet laser was fired five times at 30 Hz. A period of 4 s, after the firing of the laser, was found to be sufficient to guarantee that the fluorescent dye release was complete. At this time, an electric potential of 2000 V was applied across the 0.14 m length (142 V cm^{-1}) of a 25 μm capillary. Processed images of the resulting transport of the sample are shown to scale in figure 3(*a*) with the corresponding numerical predictions in figure 3(*b*). The uniformity of the sample in the cross-stream direction indicates purely electroosmotic/electrophoretic behavior with negligible pressure-driven effects (i.e. negligible Taylor dispersion). In the absence of these pressure-driven effects and significant Taylor dispersion, the numerical modeling could be reduced to a one-dimensional case, as opposed to the two-dimensional code used here.

Both numerically and experimentally determined centerline concentration profiles at 2/15 s intervals are shown in figure 4(*a*). The initial, far left profile was used as input into the computer code as an initial condition from which subsequent profile geometries were calculated. Despite signal noise in the peak region of the experimental profiles, the agreement is strong. As an independent check of both methods, mass conservation was verified by integrating each concentration profile. The mass contained in each experimental profile was within 2.5% of the corresponding numerical profile (all of which varied less than 0.5% from that of the initial condition). This suggests that under these experimental conditions and over this time period (<1 s), loss of fluorophores due to photo-bleaching was not significant.

The effectively diffusion-limited sample transport achieved with the pure electroosmotic flow is demonstrated in figure 4(*b*). In the figure, the initial profile is shown at

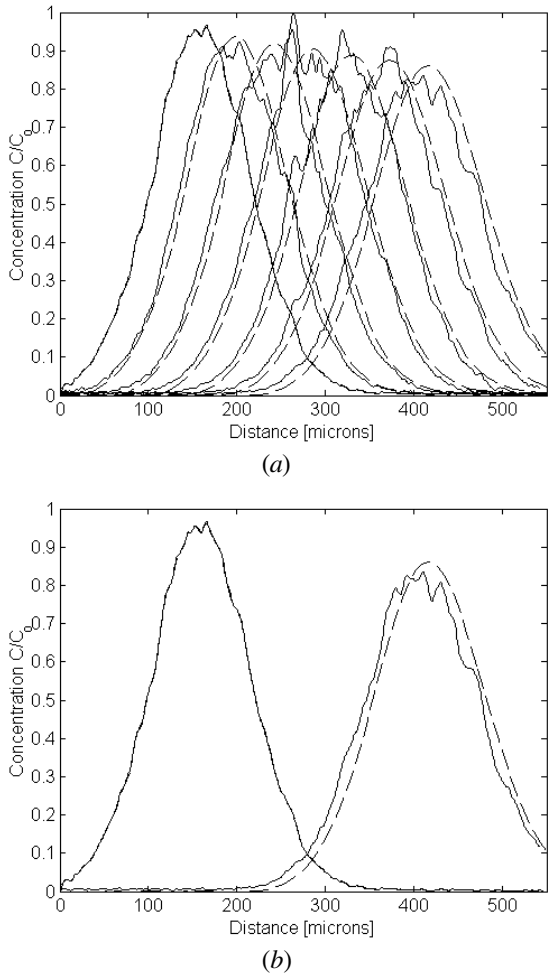

Figure 4. Experimental (solid line) and numerical (dashed line) centerline concentration profiles: (*a*) sequence of profiles at 2/15 s intervals and (*b*) initial profile, and the advected and diffused experimental profile at $t = 12/15$ s, and the superimposed numerically determined profile resulting from diffusion alone (at $t = 12/15$ s).

left, and the transported experimental profile at $t = 12/15$ s is shown at its downstream location (at right). Superimposed onto the transported profile is a numerically determined concentration profile resulting from diffusion alone (over the same time period). The close agreement between the calculated stationary profile and the actual transported experimental case indicates that diffusion-limited dispersion behavior (an ideal limit) has been effectively achieved in the transport of this sample. This proven ability effectively decouples transport speed from dispersion considerations allowing us to investigate simple diffusion of the sample as an acceptable model of sample transport. This decoupling is especially important for the experiments since the diffusion timescales are relatively long. To track a translating sample over several seconds would require a much larger field of view, resulting in a significant loss of spatial resolution.

Although the flexibility of photo-injection techniques in theory permit an infinite variety of sample geometries, here we focus on the ability to produce and transport a compact sample of uniform concentration. Towards this end, we numerically investigate the interaction of multiple uncaged samples as

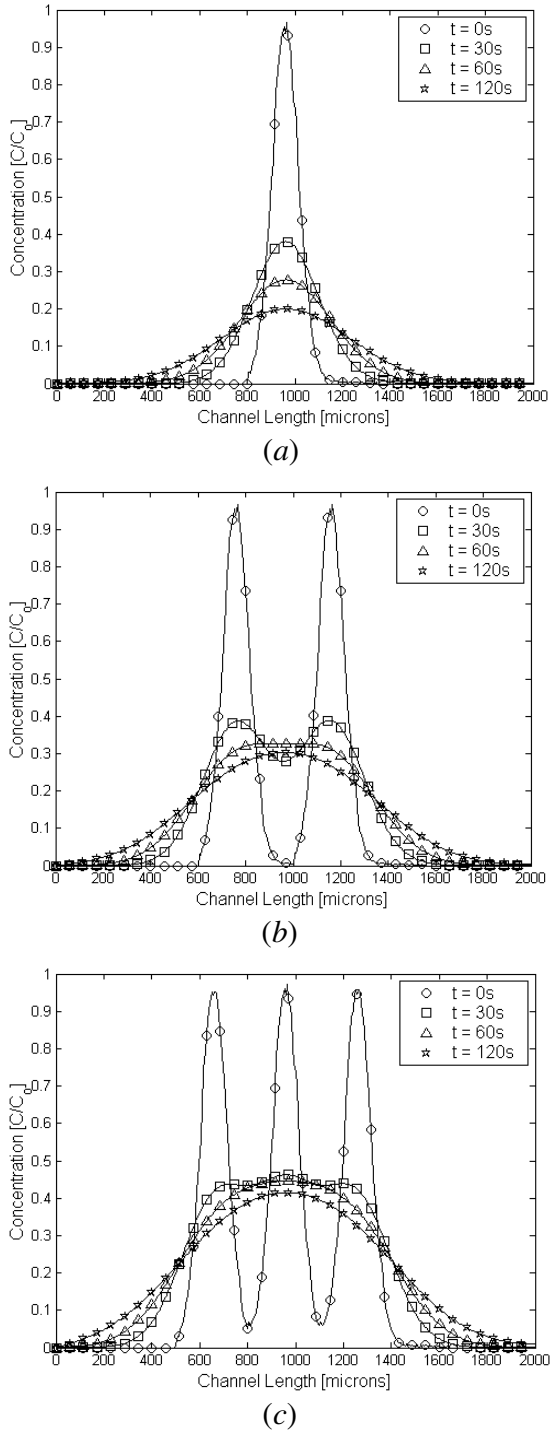

Figure 5. Numerically simulated sample diffusion interactions for: (*a*) one sample (*b*) two samples and (*c*) three samples.

a method of producing such a broad uniform concentration profile. Figures 5(*a*)–(*c*) show the results of these calculations for one, two and three samples respectively. The diffusive interactions of the multiple sample cases, shown in figures 5(*b*) and (*c*), have produced a relatively uniform concentration profile over a broad range relative to the total sample width. A sequence of the simulated two-sample diffusion interaction at 10 s intervals in perspective view is given in figure 6.

To inject a double sample in the experiments, the ultraviolet beam shaping optics were adjusted to increase the

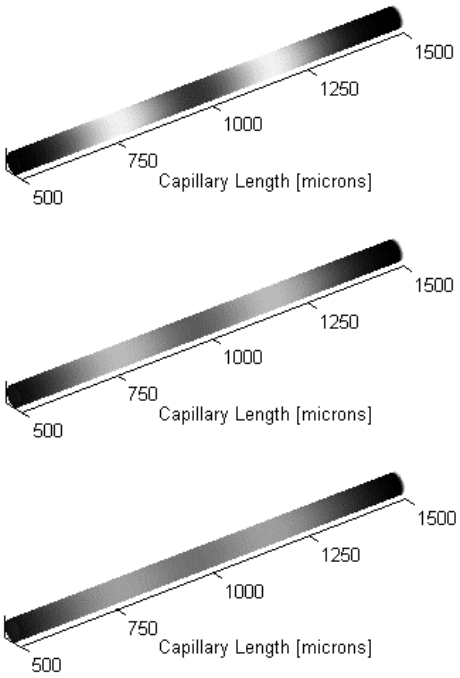

Figure 6. Perspective views of numerically simulated two-sample diffusion interaction at 10 s intervals.

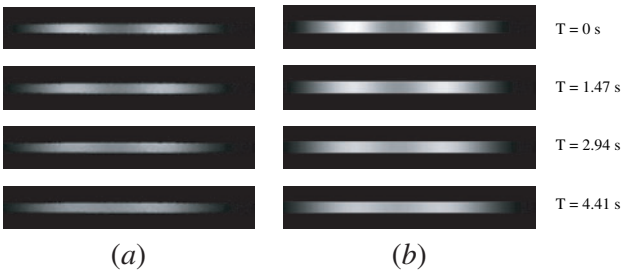

Figure 7. Processed image sequence of double-injected fluorescein sample diffusion in a 25 μm diameter capillary (sequence of images shown at 1.47 s intervals): (*a*) experimental results and (*b*) numerical predictions.

beam width at the capillary and an obstruction was inserted to divide the beam in half in the downstream direction. Due to the increased coverage area, and loss of power due to the obstruction, the laser was pulsed 15 times at 30 Hz to inject the double sample. Figure 7 shows a processed image sequence of the diffusion of the double-injected samples produced. Centerline concentration profiles determined both numerically and experimentally are given in figure 8. As before, the initial profile (at $t = 0$) was used as input into the computer code. The later times in figures 8(*b*) and (*c*) show that the two Gaussian profiles diffuse into a flat-topped concentration profile. A slight drift velocity to the left is apparent in the experimental profiles. However, since the observation time here spans several seconds, a fluid velocity as low as 2 μm s^{-1} could have caused this. Such a low fluid velocity could be caused by sub-millimeter meniscus height difference between reservoirs. A small reduction in the width of the experimental profile, as compared to the numerically determined profile, is also detectable. This could be due to photo-bleaching of the fluorophore resulting in an apparent mass loss, which can result from the prolonged exposure to

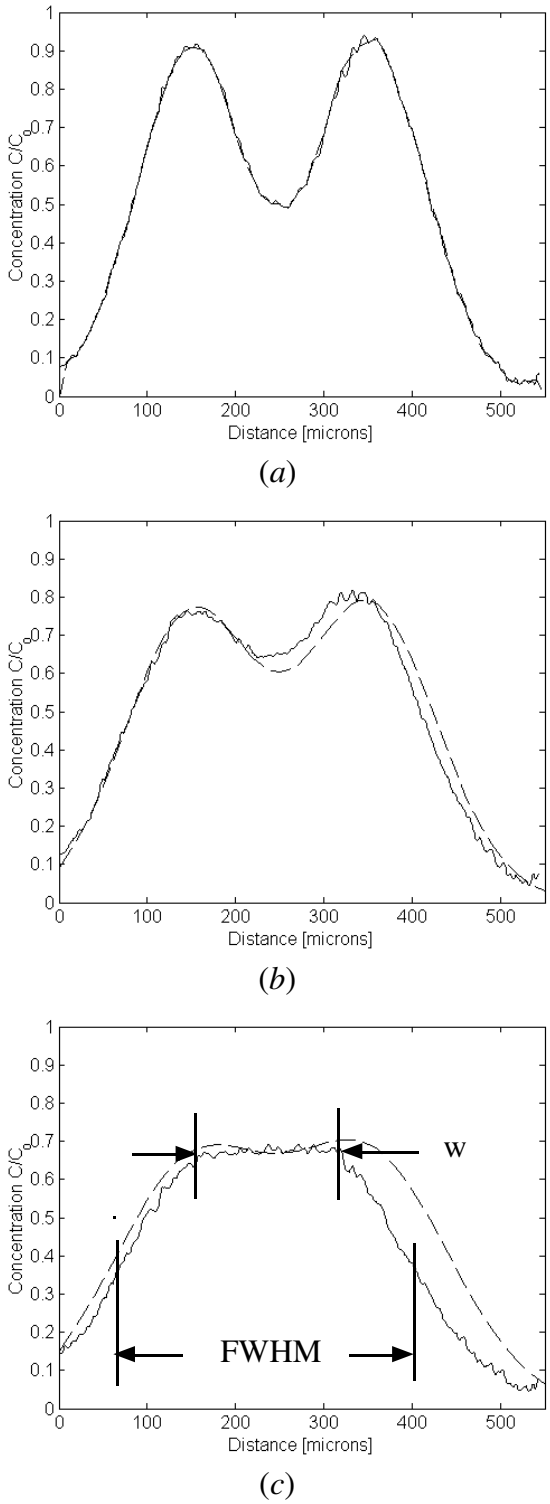

Figure 8. Experimental (solid line) and numerically determined (dashed line) centerline concentration profiles at: (a) $t = 0$ s; (b) $t = 2.9$ s and (*c*) $t = 7.3$ s (the width of the plateau region, w, and the full width at half maximum, FWHM, are shown for the experimental profile).

the excitation light. Neither of these effects were detectable in the experimental transported sample profiles presented in figures 3 and 4. This is because the time span considered was much less (<1 s) in these cases, as opposed to the profiles presented in figure 8 which span over 7 s. The apparent

mass loss is primarily a product of the stagnant flow and this specific imaging technique employed. They would not likely be present when the presented profile design was used in a sample injection in a transport application. Of interest is the extent to which a 'box-like' sample profile was achieved. The experimentally determined profile in figure 8(*c*) exhibits a mid-section of width $w = 155\ \mu$m with just a 2.5% variation in concentration. This represents a plateau extending over 45% of the sample width (determined by the full width at half maximum—FWHM).

In general, the time required to inject the sample will vary depending on the photo-injection method and photo-liable compound used. However, the time from the once-formed sample profile ($t = 0$) to the flat-topped concentration profile was found to be over 7 s, which is sufficient for a transport distance on the order of millimeters under typical circumstances (exact distance depends on the field applied and the specific combination electrophoretic and electroosmotic mobility). Given the electroosmotic velocity, the desired initial sample geometry could be calculated such that the profile arrives at its desired on-chip destination with the desired, constant concentration plateau shape.

5. Conclusions

Control over injections and reactions and effective transport of concentration-dense samples is of major importance in microfluidic technologies. Using electroosmotic flow under specific conditions, we demonstrate the ability to transport samples with diffusion-limited dispersion. Through numerical simulations we have qualitatively shown how the diffusive interaction of multiple samples can result in a non-Gaussian sample profile exhibiting a uniform concentration over a large distance. The ability to produce this sample design using photo injection was demonstrated experimentally. A profile with a constant concentration plateau varying only 2.5% over 45% of the sample width (FWHM) was presented. More generally, it was shown that photo-injection methods, in conjunction with diffusion, could be used to generate custom sample concentration profiles.

Acknowledgment

Financial support of this work by the Natural Sciences and Engineering Research Council (NSERC) of Canada, through post-graduate scholarships to DS and DE and a research grant to DL, is gratefully acknowledged.

References

[1] Blau K 1993 *Handbook of Derivatives in Chromatography* 2nd edn, ed K Blau and J M Halket (New York: Wiley)

[2] Lores M 1999 Post-column photochemical derivatization in high-performance liquid chromatography *TRAC-Trend. Anal. Chem.* **18** 392–400

[3] Deruiter C, Bohle J F, Dejong G J, Brinkman U A T and Frei R W 1998 Enhanced fluorescent detection of dansyl derivatives of phenolic-compounds using a postcolumn photochemical reactor and application to chlorophenols in river water *Anal. Chem.* **60** 666–70

[4] Gatti R, Gioia M G, Di Pietra A M and Cavrini V 2001 Analysis of phenols in pharmaceuticals by liquid chromatography after precolumn labelling and on-line postcolumn photochemical derivatization *Anal. Chim. Acta* **447** 89–99

[5] Di Pietra A M, Andrisano V, Gotti R and Cavrini V 1996 On-line post-column photochemical derivatization in liquid chromatographic-diode-array detection analysis of binary drug mixtures *J. Pharmaceut. Biomed.* **14** 1191–9

[6] Ermakov S V, Jacobson S C and Ramsey J M 1998 Computer simulations of electrokinetic transport in microfabricated channel structures *Anal. Chem.* **70** 4494–504

[7] Crabtree J H, Cheong C S, Tilroe D A and Backhouse C J 2001 Microchip injection and separation anomalies due to pressure effects *Anal. Chem.* **73** 4079–86

[8] Lempert W R, Magee K, Ronney P, Gee K R and Haugland R P 1995 Flow tagging velocimetry in incompressible flow using photo-activated nonintrusive tracking of molecular motion (PHANTOMM) *Exp. Fluids* **18** 249–57

[9] Paul P H, Garguilo M G and Rakestraw D J 1998 Imaging of pressure- and electrokinetically driven flows through open capillaries *Anal. Chem.* **70** 2459–67

[10] Herr A E, Molho J I, Santiago J G, Mungal M G, Kenny T W and Garguilo M G 2000 Electroosmotic capillary flow with non-uniform zeta potential *Anal. Chem.* **72** 1053–7

[11] Ross D, Johnson T J and Locascio L E 2001 Imaging of electroosmotic flow in plastic microchannels *Anal. Chem.* **73** 2509–15

[12] Dertinger S K W, Chiu D T, Jeon N L and Whitesides G M 2001 Generation of gradients having complex shapes using microfluidic networks *Anal. Chem.* **73** 1240–6

[13] Taylor G I 1953 Dispersion of soluble matter in solvent flowing slowly through a tube *Proc. R. Soc.* A **219** 186–203

[14] Masliyah J H 1994 *Electrokinetic Transport Phenomena* (Edmonton, Canada: AOSTRA)

[15] Inoue S and Spring K R 1997 *Video Microscopy the Fundamentals* 2nd edn (New York: Plenum)

[16] Bianchi F, Ferrigno R and Girault H H 2000 Finite element simulation of an electroosmotic-driven flow division at a t-junction of microscale dimensions *Anal. Chem.* **72** 1987–93

[17] Patankar N A and Hu H H 1998 Numerical simulation of electroosmotic flow *Anal. Chem.* **70** 1870–81

[18] Erickson D and Li D 2002 Numerical simulations of a low power microchannel thermal cycling reactor *Int. J. Heat Mass Transfer* **43** 3759–70

[19] Erickson D and Li D 2002 Influence of surface heterogeneity on electrokinetically driven microfluidic mixing *Langmuir* **18** 1883–92

[20] Stroock A D, Weck M, Chiu D T, Huck W T S, Kenis P J A, Ismagilov R F and Whitesides G M 2000 Patterning electro-osmotic flow with patterned surface charge *Phys. Rev. Lett.* **84** 3314–7